

# Strongly Anisotropic Strain-Tunability of Excitons in Exfoliated ZrSe<sub>3</sub>

Hao Li, Gabriel Sanchez-Santolino, Sergio Puebla, Riccardo Frisenda, Abdullah M. Al-Enizi, Ayman Nafady, Roberto D'Agosta,\* and Andres Castellanos-Gomez\*

The effect of uniaxial strain on the band structure of ZrSe<sub>3</sub>, a semiconducting material with a marked in-plane structural anisotropy, is studied. By using a modified three-point bending test apparatus, thin ZrSe<sub>3</sub> flakes are subjected to uniaxial strain along different crystalline orientations monitoring the effect of strain on their optical properties through micro-reflectance spectroscopy. The obtained spectra show excitonic features that blueshift upon uniaxial tension. This shift is strongly dependent on the direction along which the strain is being applied. When the flakes are strained along the *b*-axis, the exciton peak shifts at  $\approx 60\text{--}95\text{ meV \%}^{-1}$ , while along the *a*-axis, the shift only reaches  $\approx 0\text{--}15\text{ meV \%}^{-1}$ . *Ab initio* calculations are conducted to study the influence of uniaxial strain, applied along different crystal directions, on the band structure and reflectance spectra of ZrSe<sub>3</sub>, exhibiting a remarkable agreement with the experimental results.

be adjusted by the end-user at will. Strain engineering in conventional 3D materials, in contrast, typically relies on forcing the epitaxial growth of a material onto a substrate with a given lattice parameter mismatch, providing a fixed strain that cannot be adjusted after growth. Among the different strategies to strain engineer 2D materials, the application of uniaxial strain through bending flexible substrates with a bending jig apparatus is one of the most popular approaches.<sup>[1,11,12,15–18]</sup> This method presents some issues when applied to 2D materials with in-plane anisotropic properties. Indeed, the effect of uniaxial strain along different crystal orientations is expected to modify the properties of these anisotropic 2Ds differently.


## 1. Introduction

Applying mechanical deformations has become a powerful approach to modify the vibrational, optical, and electronic properties of 2D materials.<sup>[1–7]</sup> In principle, 2D materials can sustain unprecedented strains without breaking.<sup>[8–10]</sup> Moreover, their band structures are rather strain-sensitive,<sup>[11–14]</sup> making them very suitable for strain engineering applications. In addition, 2D materials offer the possibility to apply strain in various ways (e.g., uniaxial/biaxial, homogenous/inhomogenous), which can

Despite the recent interest on these families of anisotropic 2D materials,<sup>[19–26]</sup> the number of reported research works focused on studying the effect of strain along different crystal directions is still very scarce and primarily focused on the investigation of strain tunable Raman modes in black phosphorus, PdSe<sub>2</sub>, or tellurium.<sup>[27–31]</sup> The group IV–V transition metal trichalcogenides (TMTCs) are a less-explored family of materials with quasi-1D electrical and optical properties stemming from a reduced in-plane structural symmetry.<sup>[24,32–34]</sup> These materials have a general formula of MX<sub>3</sub> being M a transition metal atom

H. Li, S. Puebla, R. Frisenda, A. Castellanos-Gomez  
Materials Science Factory  
Instituto de Ciencia de Materiales de Madrid (ICMM-CSIC)  
Madrid E-28049, Spain  
E-mail: Andres.castellanos@csic.es

G. Sanchez-Santolino  
GFMC  
Departamento de Física de Materiales & Instituto Pluridisciplinar  
Universidad Complutense de Madrid  
Madrid 28040, Spain

 The ORCID identification number(s) for the author(s) of this article can be found under <https://doi.org/10.1002/adma.202103571>.

© 2021 The Authors. Advanced Materials published by Wiley-VCH GmbH. This is an open access article under the terms of the Creative Commons Attribution License, which permits use, distribution and reproduction in any medium, provided the original work is properly cited.

A. M. Al-Enizi, A. Nafady  
Department of Chemistry  
College of Science  
King Saud University  
Riyadh 11451, Saudi Arabia  
R. D'Agosta  
Nano-Bio Spectroscopy Group and European Theoretical Spectroscopy Facility (ETSF)  
Departamento de Polímeros y Materiales Avanzados: Física  
Química y Tecnología  
Universidad del País Vasco UPV/EHU  
Avenida Tolosa 72, San Sebastián E-20018, Spain  
E-mail: roberto.dagosta@ehu.es

R. D'Agosta  
IKERBASQUE  
Basque Foundation for Science  
Plaza Euskadi 5, Bilbao E-48009, Spain

DOI: 10.1002/adma.202103571

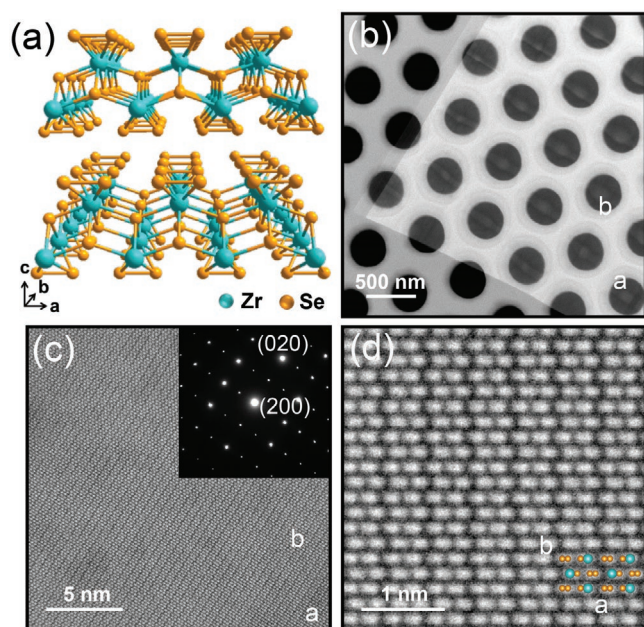


**Figure 1.** Structural characterization of  $\text{ZrSe}_3$ . a) 3D representation of the crystal structure of  $\text{ZrSe}_3$  where the in-plane anisotropy can be resolved. b,c) Low magnification and atomic resolution HAADF images of a mechanically exfoliated  $\text{ZrSe}_3$  flake transferred over a holey  $\text{Si}_3\text{N}_4$  membrane. The inset in (c) shows an SAED pattern acquired at the same region; d) Atomic resolution HAADF image of the  $\text{ZrSe}_3$  flake down the (001) direction depicting the chains-like structure along the  $b$ -axis. The superimposed atomic model depicts the Zr (cyan) and Se (orange) atomic column positions.

belonging to either group IVB (Ti, Zr, Hf) or group VB (Nb, Ta) and X chalcogen atoms from group VIA (S, Se, Te).

In this work, we focused on  $\text{ZrSe}_3$ , a semiconductor of the transition metal trichalcogenide family<sup>[24]</sup> with a strong in-plane anisotropic structure similar to that of  $\text{TiS}_3$ ,<sup>[35–38]</sup> along different crystal directions (see **Figure 1a**).  $\text{ZrSe}_3$  has been scarcely studied experimentally so far. Xiong et al. presented a photodetector based on individual  $\text{ZrSe}_3$  nanobelts<sup>[39]</sup> and Zhou et al. proposed its potential application in thermoelectrics through calculations,<sup>[40]</sup> but little is still known about the fundamental electronic and optical properties of this semiconducting material. We explored how applying strain along different crystal orientations modifies the excitonic features in the optical spectra. Our straining technique relies on a three-point bending test apparatus, and it can be easily adapted by other groups that are already working on strain engineering of 2D materials. Using this straining approach, we demonstrate how the direction along which we apply the uniaxial strain has a strong effect on the strain tunability of the excitonic features on this anisotropic 2D material. Evidently, a giant anisotropy in the strain-induced exciton shift was found. The strain gauge factor varies from  $\approx 60$  to  $95 \text{ meV } \%^{-1}$  for uniaxial strain applied along the  $b$ -axis to  $\approx 0$ – $15 \text{ meV } \%^{-1}$  when the uniaxial strain is applied along the  $a$ -axis. Additionally, ab initio calculations were performed, supporting the finding of the strongly anisotropic strain-tunable direct band-gap transitions observed in the experiments. Therefore, being able to accurately align the direction of the uniaxial strain axis with specific crystalline orientations is strongly

appealing to further employ this family of 2D materials in strain engineering applications.

## 2. Sample Fabrication and Straining Setup

$\text{ZrSe}_3$  flakes are obtained by mechanical exfoliation of bulk crystals and transferred through an all-dry deterministic placement method<sup>[41–43]</sup> (see the Experimental Section). **Figure 1b** shows a high-angle annular dark-field scanning transmission electron microscopy (HAADF-STEM) image of a thin  $\text{ZrSe}_3$  flake transferred onto a holey  $\text{Si}_3\text{N}_4$  TEM grid to characterize its crystal structure. **Figure 1c** shows an atomic resolution HAADF image of the same flake along the (001) direction, in which the anisotropic in-plane structure of  $\text{ZrSe}_3$  is visible. The inset shows a selected area electron diffraction (SAED) pattern acquired at the same region corresponding to a monoclinic ( $P2_1/m$ ) crystal structure. A high magnification atomic resolution HAADF image shown in **Figure 1d** clearly illustrates the chain-like structure of  $\text{ZrSe}_3$  within the  $a$ – $b$  plane, similar to that of  $\text{TiS}_3$ .<sup>[24]</sup>

The angle-dependent uniaxial strain measurements are based on the integration of disk-shaped flexible substrates, instead of the commonly used rectangular beam, in a bending-test apparatus. **Figure 2a** is a schematic representation of the fabrication process. The samples are fabricated out of a disk-shaped polycarbonate substrate (thickness =  $250 \mu\text{m}$ ). Permanent marker lines are drawn on the surface to guide the angle adjustment. The  $\text{ZrSe}_3$  flakes are then transferred onto the geometrical center of the disk surface by means of an all-dry deterministic placement method with an accuracy of  $\approx 10 \mu\text{m}$ .<sup>[41–43]</sup>

The disk-shaped substrate with the  $\text{ZrSe}_3$  is then loaded in a homebuilt three-point bending jig apparatus to apply uniaxial strain through bending of the substrate (**Figure 2b,c**).<sup>[15]</sup> After a strain load/unload cycle, the disk-shaped sample can be rotated to apply uniaxial strain along another direction. **Figure 2d**,e shows an example where uniaxial strain is applied along two orthogonal directions (notice the position of the red marker line). The amount of strain can be extracted from the geometry of the disk substrate and the bending apparatus through

$$\varepsilon = \frac{6tD}{L^2} \quad (1)$$

where  $t$  is the thickness of the substrate,  $L$  is the distance between the outer pivotal points, and  $D$  is the deflection of the central pivotal point (see **Figure 2c**). Note that we have experimentally validated this formula to calculate the strain in ref. [15] by directly measuring the separation of micro-fabricated features in the surface of the polycarbonate substrates upon controlled deflection of the substrate with the three-point bending apparatus.

## 3. Results

**Figure 3a** displays an optical microscopy image of a  $\approx 16 \text{ nm}$  thick  $\text{ZrSe}_3$  flake (see **Figure S1**, Supporting Information),

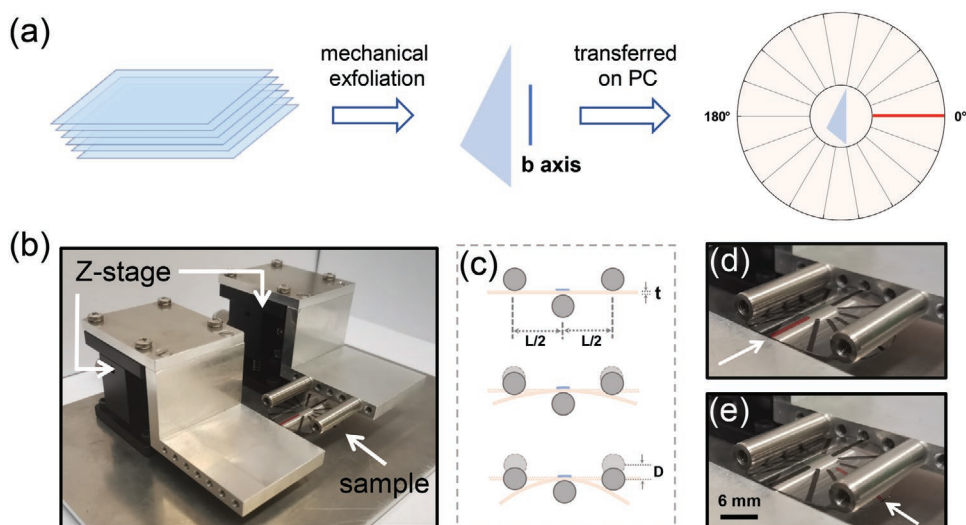


**Figure 2.** Setup for angle-resolved uniaxial straining measurements. a) Cartoon of the fabrication process of the test sample. A disk-shaped polycarbonate substrate is marked with a permanent marker every 20° angle from 0°–360°, highlighting the 0° with a red line. An exfoliated ZrSe<sub>3</sub> flake is then transferred onto the center of the disk by an all-dry deterministic placement method. b) Picture of the three-points bending setup used for the strain engineering experiments with a disk-shaped flexible substrate loaded between the pivotal points. c) Schematic representation of the three-point bending process. d,e) Pictures of the sample upon 0.65% of uniaxial strain applied along two orthogonal directions (notice the position of the red marker line).

transferred onto the center of a disk-shaped flexible polycarbonate substrate. For the angle-dependent uniaxial straining experiments, it is crucial to accurately determine the crystal orientation of the ZrSe<sub>3</sub> flake under study. This can be done by measuring reflection or absorption spectra with linearly

polarized incident light. When the incident light is linearly polarized along the *b*-axis, the spectra show prominent excitonic features, even at room temperature.<sup>[44,45]</sup> When the light is polarized along the *a*-axis, on the other hand, the intensity of these excitonic features decreases substantially.

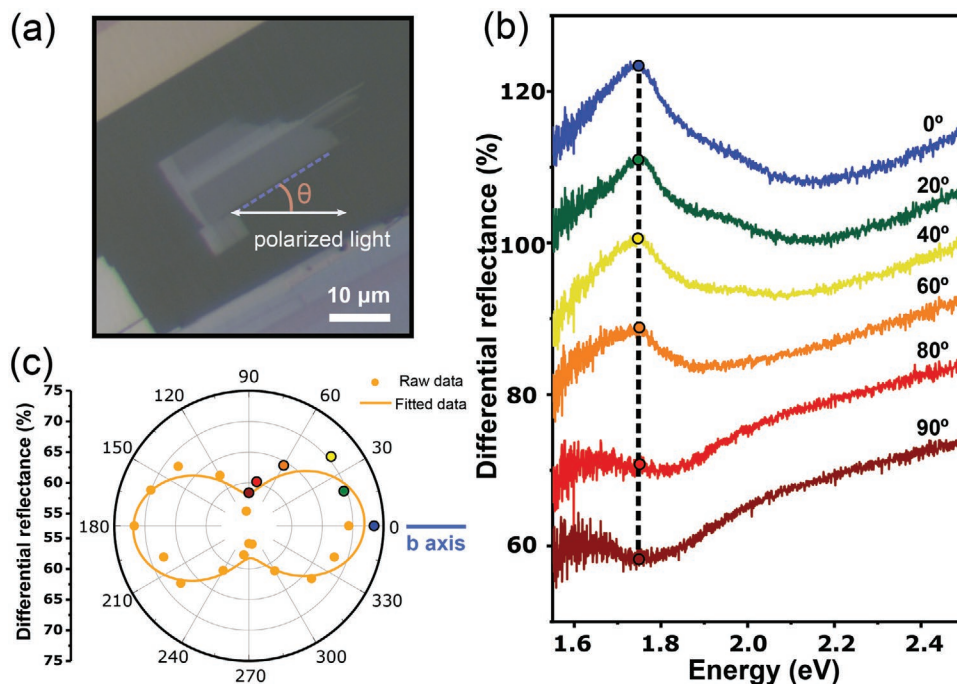


**Figure 3.** Identification of crystalline orientations of ZrSe<sub>3</sub>. a) Optical microscopy image of a few-layer ZrSe<sub>3</sub> flake. In the angle-resolved measurements,  $\theta$  is defined as the angle between the cleaved long straight edge of the flake (dashed blue line) and the polarization direction (parallel to the horizontal axis of the microscope, white arrow). b) Micro-reflectance spectra of the ZrSe<sub>3</sub> flake (unstrained) as a function of sample rotation angle from 0° to 90° while the incident light is linearly polarized parallel to the horizontal axis. The spectra have been vertically offset by 10% to facilitate the comparison. c) Polar plot of the differential reflectance intensity at  $\approx 1.75$  eV for different angles between the incident linearly polarized light and the cleaved long straight edge of the ZrSe<sub>3</sub> flake. The color circles correspond to the spectra shown in (b).



We have used a homebuilt differential reflectance system to acquire reflectance spectra with linearly polarized incident light to determine the ZrSe<sub>3</sub> crystal orientation.<sup>[46,47]</sup> We found that other optical spectroscopic techniques, like photoluminescence or Raman spectroscopy, could not be carried out in the ZrSe<sub>3</sub> due to laser-induced damage of the flakes even at very low laser power density values ( $\approx 40 \mu\text{W} \mu\text{m}^{-2}$ ). Figure S2 in the Supporting Information shows the damage caused by the laser when attempting to carry out Raman spectroscopy and photoluminescence measurements with low excitation power. In our differential reflectance experiments, we fixed the incident light linearly polarized parallel to the horizontal axis of the microscope while the ZrSe<sub>3</sub> flake is rotated to vary the orientation between the linearly polarized light and the crystal axes. Figure 3b shows differential reflectance spectra acquired for different angles ( $\theta$ ) between the incident linearly polarized light and the long cleaved edge of the ZrSe<sub>3</sub> flake (highlighted with a dashed blue line in Figure 3a). When the straight long edge of the flake is parallel to the linearly polarized light (labeled as 0° or 180°), the spectra show a broad peak feature at  $\approx 1.75$  eV and a shoulder at  $\approx 1.9$  eV. These peaks are attributed to the generation of excitons (called A and B in the literature, respectively) due to direct valence-to-conduction band transitions.<sup>[44,45]</sup> The intensity of these excitonic peaks decreases when the flake is rotated and it reaches its minimum intensity when the long edge of the flake is perpendicular to the incident linearly polarized light. This observation indicates that the *b*-axis of the ZrSe<sub>3</sub> flake is oriented parallel to the long edge of the flake.<sup>[44,45]</sup> Figure 3c represents the intensity of the A exciton peak at different angles between the incident linearly polarized light and the long straight edge of the flake. The polar plot clearly illustrates how the intensity of the exciton feature reaches its maximum value when the long edge of the flake is aligned parallel to the incident polarized light (horizontal axis).

After determining the crystal orientations of the ZrSe<sub>3</sub> flake under study, we subject it to uniaxial strain cycles. Differential reflectance spectroscopy at different strain values was conducted to infer the effect of strain on the excitonic features of the optical spectra. After each uniaxial strain cycle, the disk-shaped substrate is rotated by  $\approx 20^\circ$ , changing the angle ( $\theta$ ) between the crystal *b*-axis and the uniaxial strain direction. We label as 0°/180° the situation where the uniaxial strain is parallel to the *b*-axis and 90°/270° the one where the uniaxial strain is perpendicular to the *b*-axis. For this experiment, the incident polarized light is kept parallel to the *b*-axis to maximize the intensity of the exciton peaks but comparable results are obtained using unpolarized light (see Figure S4, Supporting Information).

Figure 4a shows a selection of differential reflectance spectra acquired while applying different uniaxial strain values almost parallel to the *b*-axis ( $\theta = 2^\circ$ ). Figure 4b shows other differential reflectance spectra versus strain acquired when the uniaxial strain is orthogonal to the *b*-axis ( $\theta = 90^\circ$ ). Note that a smooth polynomial background has been subtracted from the spectra to facilitate identifying the exciton peaks (see Figure S3 in the Supporting Information that compares some spectra before and after removing the background). The spectra have been fitted to a sum of two Gaussian peaks to accurately determine

the energy of the A and B excitonic features. Figure 4c summarizes the A exciton peak energy versus uniaxial strain acquired for different alignment between the uniaxial straining direction and the ZrSe<sub>3</sub> *b*-axis. The strain gauge factor, defined as the spectral shift per % of uniaxial strain, strongly depends on the angle between the uniaxial straining direction and the *b*-axis. It ranges from  $\approx 95 \text{ meV} \%^{-1}$  for parallel configuration ( $\theta = 2^\circ$ ) to  $\approx 15 \text{ meV} \%^{-1}$  for the orthogonal configuration ( $\theta = 90^\circ$ ). Figure 4d further summarizes the gauge factors determined for different alignment between the uniaxial strain direction and the ZrSe<sub>3</sub> *b*-axis.

The B exciton peak is much lower in intensity and it is wider, making the Gaussian fit less accurate. This motivated us to focus on the A exciton, that contains information about the lower energy direct band-to-band transition. Nonetheless, we address the reader to Figure S5 in the Supporting Information for a dataset where both A and B exciton energies have been determined as a function of strain. Figure S5 in the Supporting Information also shows the effect of compressive uniaxial strain (using a four-points bending setup, see Scheme S1, Supporting Information) on the differential reflectance of a ZrSe<sub>3</sub> flake, showing how the A and B exciton peaks redshift upon compression at a rate of  $\approx -80 \text{ meV} \%^{-1}$ .

It is worth noting that the ZrSe<sub>3</sub> gauge factor for uniaxial strain along the *b*-axis is substantially larger than that of transition metal dichalcogenides (typically in the  $30\text{--}60 \text{ meV} \%^{-1}$ )<sup>[15]</sup> and reproducible (see Figure S6, Supporting Information). In fact, this value is very close to that of InSe<sup>[48,49]</sup> and black phosphorus,<sup>[29]</sup> the 2D materials with the largest strain gauge factors reported so far. However, both InSe and black phosphorus are sensitive to the environmental exposure and tend to degrade. We have found that the observed exciton strain tunability remains stable even after 4 months of exposure to atmospheric conditions (see Figures S7 to S10, Supporting Information).

We have measured a total of 11 ZrSe<sub>3</sub> flakes obtaining comparable results (see Figures S11 to S19 of the Supporting Information). This illustrates the robustness of the observed anisotropy in the strain-tunable A exciton energy. In order to get an insight about the maximum strain that the ZrSe<sub>3</sub> flakes can sustain, Flakes 7, 8, and 9 were subjected to uniaxial strain until fracture (see Figures S16–S18 in the Supporting Information), revealing that the flake breakdown occurs between  $\approx 0.8\%$  and  $1.2\%$ .

To quantify the observed anisotropy in the strain tunability of the excitons, we define the anisotropy ratio of the gauge factor as

$$\text{Anisotropy ratio} = (\text{GF}_{\text{max}} - \text{GF}_{\text{min}}) / (\text{GF}_{\text{max}} + \text{GF}_{\text{min}}) \cdot 100\% \quad (2)$$

where  $\text{GF}_{\text{min}}$  and  $\text{GF}_{\text{max}}$  stands for the minimum and maximum gauge factors, respectively. This formula gives 0% for perfectly isotropic material. For the studied ZrSe<sub>3</sub> flakes, we get values ranging from 72% to  $\approx 100\%$ . Black phosphorus, another 2D material with a remarkable in-plane structural anisotropy, showed only an  $\approx 3\%$  anisotropy ratio of the gauge factor.<sup>[29]</sup> Table 1 compares the gauge factors along different crystal directions for ZrSe<sub>3</sub> and those reported for black phosphorus in ref. [29]. Table 1 also includes information about the thickness of the ZrSe<sub>3</sub> flakes. Samples 1, 2, 6, 8, and 11 were characterized by atomic force microscopy (AFM). For the other ZrSe<sub>3</sub>

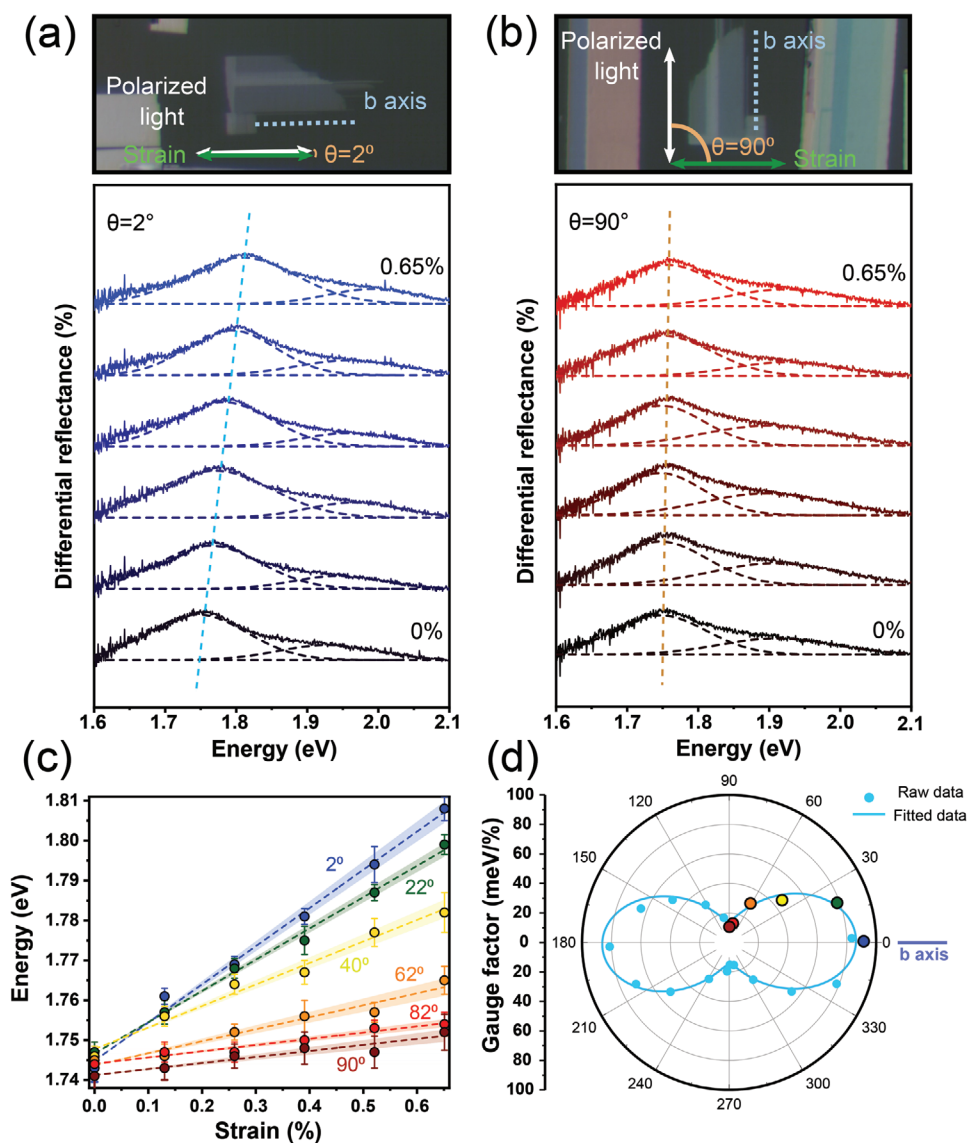


**Figure 4.** Angle-resolved micro-reflectance spectra of  $\text{ZrSe}_3$  under different uniaxial strain from 0% to 0.65%. a, b) Micro-reflectance spectra acquired when the uniaxial strain direction is parallel to the *b*-axis and the *a*-axis of the  $\text{ZrSe}_3$  flake, respectively. c) A-exciton peak energy as a function of the applied uniaxial strain under different orientation angles ( $2^\circ$ ,  $22^\circ$ ,  $40^\circ$ ,  $62^\circ$ ,  $82^\circ$ , and  $90^\circ$ ). A linear fit is used to extract the gauge factor. The shaded area around the dashed lines indicates the uncertainty in the linear fit and provides a measurement of the uncertainty of the extracted gauge factor. d) Angular dependence of the  $\text{ZrSe}_3$  A exciton gauge factor in polar coordinates. All the tests are carried out with the strain axis parallel to the horizontal axis of the microscope and by keeping the incident linearly polarized light and flake *b*-axis direction parallel to each other along the whole experiment to maximize the excitons intensities.

samples, an estimation of their thickness has been obtained from the optical contrast extracted from the red channel of the optical images (see Figure S20 in the Supporting Information for details). We have not found any clear thickness dependence in the resulting gauge factor nor anisotropy ratio. We attribute this to the fact that the thinner studied flake was  $\approx 8$  nm (approximately eight layers) that is expected to show bulk-like properties (see Figure S21, Supporting Information). At the present, we could not exfoliate thinner flakes with a large enough area to study strain engineering experiments with differential reflectance. Note that for a good strain transfer, flakes of at least  $10 \times 10 \mu\text{m}^2$  are selected.

We have also carried out ab initio calculations to investigate further this strongly anisotropic response to strain of  $\text{ZrSe}_3$ . Figure 5a shows the electronic band structure of bulk  $\text{ZrSe}_3$ , as calculated within the GW approximation for the unstrained structure and for 1% strain applied along the *a* and *b* axes. For the unstrained structure, we obtain a direct electronic band-gap of 1.29 eV at the  $\Gamma$  point, and an indirect band gap of 0.66 eV between  $\Gamma$  and X points. The GW approximation corrects the density functional theory (DFT) band gaps (direct, 0.46 eV, indirect 0.15 eV) bringing them closer to the experimental values. The main effect of the GW approximation is a rigid upward shift of the conduction bands in the whole Brillouin zone. We

**Table 1.** Summary of the reported exciton shift upon uniaxial strain along different in-plane directions for ZrSe<sub>3</sub> and black phosphorus.

Reference	Material	Thickness [nm]	Gauge factor [meV % <sup>-1</sup> ]		Anisotropy ratio [%]
			Axis 1	Axis 2	
This work	ZrSe <sub>3</sub> (Sample 1, Figure 3)	16.0 <sup>AFM</sup>	+ (15.1 ± 2.4)	+ (95.7 ± 4.1)	72.7
	ZrSe <sub>3</sub> (Sample 2, Figure S6, Supporting Information)	14.5 <sup>AFM</sup>	≈0	+ (75.7 ± 5.3)	≈100
	ZrSe <sub>3</sub> (Sample 3, Figure S7, Supporting Information)	≈8 <sup>OPT</sup>	+ (5.7 ± 3.2)	+ (70.2 ± 0.6)	84.9
	ZrSe <sub>3</sub> (Sample 4, Figure S8, Supporting Information)	≈16 <sup>OPT</sup>	+ (4.4 ± 3.9)	+ (91.7 ± 8.9)	90.8
	ZrSe <sub>3</sub> (Sample 5, Figure S9, Supporting Information)	≈16 <sup>OPT</sup>	+ (2.0 ± 2.8)	+ (82.7 ± 3.9)	95.3
	ZrSe <sub>3</sub> (Sample 6, Figure S10, Supporting Information)	8.3 <sup>AFM</sup>	+ (4.6 ± 3.0)	+ (92.0 ± 5.7)	90.5
	ZrSe <sub>3</sub> (Sample 7, Figure S11, Supporting Information)	≈16 <sup>OPT</sup>	–	+ (70.1 ± 4.0)	–
	ZrSe <sub>3</sub> (Sample 8, Figure S12, Supporting Information)	12.8 <sup>AFM</sup>	–	+ (64.1 ± 3.4)	–
	ZrSe <sub>3</sub> (Sample 8, Figure S12, Supporting Information) <sup>a)</sup>	12.8 <sup>AFM</sup>	+ (10.5 ± 4.1)	+ (77.6 ± 3.6)	76.2
	ZrSe <sub>3</sub> (Sample 9, Figure S13, Supporting Information)	≈13 <sup>OPT</sup>	–	+ (74.3 ± 5.0)	–
	ZrSe <sub>3</sub> (Sample 10, Figure S14, Supporting Information) <sup>b)</sup>	≈15 <sup>OPT</sup>	–	+ (68.7 ± 7.9) to + (81.2 ± 4.7)	–
	ZrSe <sub>3</sub> (Sample 10, Figure S5, Supporting Information) <sup>c)</sup>	≈15 <sup>OPT</sup>	–	– (78.3 ± 4.0)	–
	ZrSe <sub>3</sub> (Sample 11, Figure S5, Supporting Information) <sup>d)</sup>	14.2 <sup>AFM</sup>	+ (9.6 ± 5.0) to + (22.6 ± 5.0)	+ (83.8 ± 2.0) to + (93.0 ± 5.5)	57.5 to 81.3
	[29]	ZrSe <sub>3</sub> (ab initio)	Bulk	+ 10.9	+ 58.7
	BP	3.3	+ 117	+ 124	2.9

<sup>a)</sup>Measurement carried out 4 months after the sample fabrication (sample stored in air); <sup>b)</sup>Measurement acquired in five straining/releasing cycles; <sup>c)</sup>Measurement acquired by applying compressive strain; <sup>d)</sup>Measurements carried out at different times along 1 month of exposure to air.

clearly see that a 1% tensile strain along the *b*-axis shifts the direct band gap up by about +90 meV while the same strain along the *a*-axis only shifts the bands by +45 meV. Interestingly, the anisotropy in the strain-tunable indirect band gap is less pronounced, +100 meV %<sup>-1</sup> along the *b*-axis and +85 meV %<sup>-1</sup> along the *a*-axis, in good agreement with previously reported DFT calculations that only focused on the indirect band-gap strain tunability without considering excitonic effects.<sup>[50]</sup>

In order to directly compare with our experimental findings, we have calculated reflectance spectra (Figure 5b,c) via solving the Bethe–Salpeter’s equation (see the Experimental Section for further information). The spectra present two prominent peaks around ≈1.4 and ≈1.75 eV, due to the generation of A and B excitons respectively. These two peaks are lower in energy than the experimental values, but their positions are consistent with the smaller band gap we obtained in the GW approximation. Interestingly, our calculation also predicts the presence of another exciton, that we label as B\*, with an energy between that of A and B excitons but with a very low intensity. Figure 5a includes a zoomed-in plot of the band structure, indicating the different band-to-band transitions that originate the A, B, and B\* excitons.

We calculated the effect of tensile strain along the *a*- and *b*-axis, considering incident light polarized along the *b*-axis of ZrSe<sub>3</sub>. For the strain along the *b*-axis, we clearly observe a blueshift of the exciton peaks (at a rate of ≈59 meV %<sup>-1</sup> of uniaxial strain for the A exciton), consistent with an increase in the electronic band gap. The exciton blueshift is much less pronounced (only ≈11 meV %<sup>-1</sup> for the A exciton) when uniaxial strain is applied along the *a*-axis, reflecting the minimal effect of strain applied along that crystal direction on the band structure. In order to get an insight about the physical origin of the anisotropy in the strain-tunable exciton energies, we have analyzed the contribution of the different atoms, and their orbitals,

to the band structure (see Figures S22 to S24 in the Supporting Information and related discussion). Our analysis allows us to conclude that the conduction bands, around  $\Gamma$ , are mainly determined by the Zr  $d_{xy}$  and  $d_{yz}$  orbitals. This fact suggests that deforming the unit cell along  $\gamma$  (*b*-axis) might have a more significant impact since it modifies the bonds containing the  $d_{xy}$  and  $d_{yz}$  orbitals (see Figure S25 in the Supporting Information). At the same time, a deformation along  $x$  (*a*-axis) only affects the  $d_{xz}$  orbital. Regarding the valence band maximum around the  $\Gamma$  point, our analysis concludes that it is mainly determined by the  $p_z$  orbital of Se<sub>2</sub> atoms. This observation explains rather the insensitiveness of the valence band maximum to strain applied to both the *a* and *b* directions (parallel to  $x$  and  $\gamma$  in our case) as pointed out by our band structure calculations.

Note that the theoretical anisotropy ratio is ≈69%, slightly lower than the experimental values that span from 72% to nearly 100%. We attribute this underestimation of the anisotropy to the fact that we neglected the Poisson’s effect in our calculation as we could not find any previously peer-reviewed reported value of the Poisson’s ratio of ZrSe<sub>3</sub>. According to the Poisson’s effect, a tensile strain along the *a*-axis will be accompanied by a small compression along the *b*-axis that could effectively reduce the exciton strain-induced shift. In fact, a compression along *b*-axis will lead to a redshift of the excitons (see Figure S5 of the Supporting Information) which could partially compensate the blueshift produced by the tension along the *a*-axis, thus increasing the anisotropy ratio.

## 4. Conclusions

In summary, we subjected thin ZrSe<sub>3</sub> flakes to uniaxial strain along different crystal orientations. We found that the

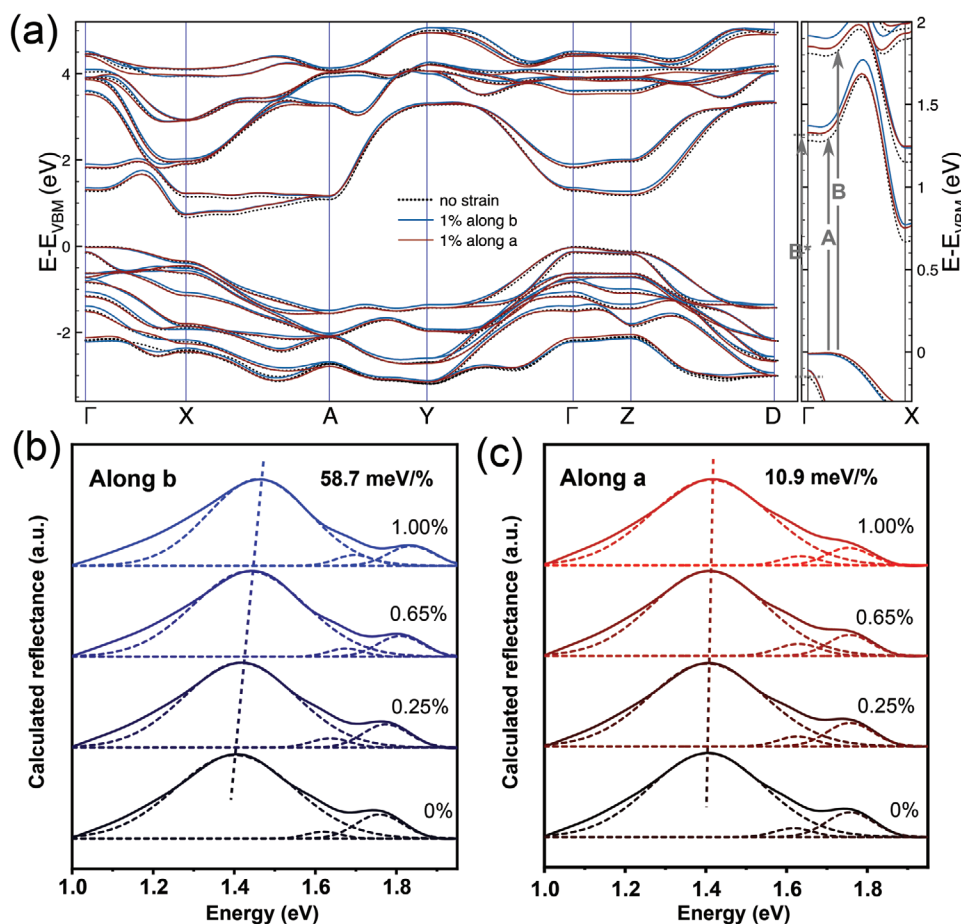


**Figure 5.** Calculated band structure and reflectance spectra for uniaxial strains along the  $b$ - and  $a$ -axis. a) Band structure, calculated within the GW approximation, for different straining situations: 0% strain (dotted black), +1% uniaxial strain along  $a$ -axis (red), and +1% uniaxial strain along  $b$ -axis (blue). We have selected the path in the first Brillouin zone:  $\Gamma = (0,0,0)$ ,  $X = (\frac{1}{2},0,0)$ ,  $A = (\frac{1}{2},\frac{1}{2},0)$ ,  $Y = (0,\frac{1}{2},0)$ ,  $Z = (0,0,\frac{1}{2})$ ,  $D = (0,\frac{1}{2},\frac{1}{2})$ . A zoomed-in region in the  $\Gamma$ - $X$  has been plotted to highlight the direct band-to-band transitions that originate the A, B, and  $B^*$  excitons. b,c) Calculated reflectance spectra (solid lines) for different uniaxial tensile strains along the  $b$ -axis (blue) and  $a$ -axis (red), respectively. The dashed lines represent a fit with three Gaussian functions to determine the position of the A, B, and  $B^*$  exciton peaks.

reflectance spectra showed a peak, associated with a direct band gap transition, that blueshifts upon uniaxial tension, indicating a tension-induced band gap increase. Interestingly, the spectra shift rate strongly depends on the direction along which the strain is being applied. While strain along the  $b$ -axis yielded a spectral shift up to  $\approx 60$ – $95$  meV  $\%^{-1}$ , strain applied along the  $a$ -axis only yielded a shift of  $\approx 0$ – $15$  meV  $\%^{-1}$ . Ab initio calculations further verified the large anisotropic strain-tunable band-gap transitions observed in our experiments.

## 5. Experimental Section

**Sample Fabrication:** Bulk  $ZrSe_3$  crystals (from HQ Graphene) were exfoliated with Nitto SPV 224 tape and transferred to a Gel-Film (Gel-Pak WF  $\times$  4 6.0 mil) substrate. Then, the surface of the Gel-Film substrate was scanned under an optical microscope operated in transmission mode to identify the flakes. Once the desired flake was identified, it could be transferred onto a desired location of a target substrate by means of an all-dry deterministic placement method.<sup>[41–43]</sup>

**Strain-Dependent Differential Reflectance Spectroscopy:** The disk-shaped flexible substrate containing the desired flake on its center was loaded into the three-points bending system and the whole system was mounted under the objective of an optical microscope (Motic BA310 Met-T) system supplemented with a homebuilt micro-reflectance module based on a fiber-coupled CCD spectrometer (CCS200/M, Thorlabs) as previously reported.<sup>[46]</sup> The assigned flake was centered with respect to the central pivot using microscope inspection. Importantly, differential reflectance was used instead of photoluminescence, commonly employed to monitor the effect of strain on the optical properties of 2D semiconductors, given that photoluminescence measurements led to a laser-induced burning of thin  $ZrSe_3$  flakes.

**Ab Initio Calculations:** The electronic band structure and the optical reflectance were calculated through the GW approximation starting from DFT calculations. The atomic structure was initially relaxed, until the residual force between the atoms was below  $4.0 \times 10^{-4}$  eV  $\text{\AA}^{-1}$ . The lattice parameters,  $a = 5.44$   $\text{\AA}$ ,  $b = 3.73$   $\text{\AA}$ , and  $c = 9.45$   $\text{\AA}$  with an angle between  $a$  and  $c$  of  $97.6^\circ$  were determined. All calculations were performed with scalar relativistic generalized gradient approximation-Perdew–Burke–Ernzerhof pseudopotentials in the optimized norm-conserving Vanderbilt set.<sup>[51,52]</sup> The Quantum Espresso suite was used for the calculations.<sup>[53,54]</sup> An energy cut-off of  $10^3$  eV and a uniform mesh of  $k$ -points of  $6 \times 6 \times 6$  in the Brillouin zone were set. The GW calculations were performed



using the Yambo code<sup>[55,56]</sup> starting from the Quantum Espresso output. The optical spectra were obtained by solving the Bethe–Salpeter equation starting from the GW calculation in the plasmon-pole approximation. This calculation provided the real and imaginary part of the dielectric function of the material. From there, the reflectance was evaluated considering that the light was perpendicular to the sample. The line width of the spectra was therefore obtained from the solution of that equation without any further approximation. In particular, the method was able to evaluate the electronic self-energy thus providing the line width. After modifying the unit cell parameters to take into account the uniaxial strain, the atomic position was optimized till the residual force was below  $4.0 \times 10^{-4}$  eV Å<sup>-1</sup>.

**Scanning Transmission Electron Microscopy (STEM):** For STEM characterization, ZrSe<sub>3</sub> flakes were mechanically transferred onto a holey Si<sub>3</sub>N<sub>4</sub> membrane and characterized using an aberration-corrected JEOL JEM-ARM 200cF electron microscope equipped with a cold field emission gun and operated at 80 kV.

## Supporting Information

Supporting Information is available from the Wiley Online Library or from the author.

## Acknowledgements

This project was funded from the European Research Council (ERC) under the European Union's Horizon 2020 research and innovation program (grant agreement no. 755655, ERC-StG 2017 project 2D-TOPSENSE). R.F. acknowledges the support from the Spanish Ministry of Economy, Industry and Competitiveness through a Juan de la Cierva-formation fellowship 2017 FJCI2017-32919. R.D. acknowledges the financial support of the Grupos Consolidados del Gobierno Vasco (Grant IT1249-19) and the MINECO (Grant G17/A01). G.S.-S. acknowledges financial support from Spanish MICIU RTI2018-099054-J-I00 and MICINN IJC2018-038164-I. Electron microscopy observations were carried out at the Centro Nacional de Microscopia Electronica, CNME-UCM. R.D. also acknowledges useful discussions with D. Varsano. H.L. acknowledges the grant from China Scholarship Council (CSC) under no. 201907040070. The authors extend their sincere appreciation to the Distinguished Scientist Fellowship Program (DSFP) at King Saud University for funding of this work.

## Conflict of Interest

The authors declare no conflict of interest.

## Data Availability Statement

Research data are not shared.

## Keywords

2D materials, anisotropy, band-gap engineering, strain engineering, zirconium triselenide (ZrSe<sub>3</sub>)

Received: May 11, 2021

Revised: September 24, 2021

Published online: October 15, 2021

[1] R. Roldán, A. Castellanos-Gomez, E. Cappelluti, F. Guinea, *J. Phys.: Condens. Matter* **2015**, *27*, 313201.

[2] B. Amorim, A. Cortijo, F. de Juan, A. G. Grushin, F. Guinea, A. Gutiérrez-Rubio, H. Ochoa, V. Parente, R. Roldán, P. San-Jose,

J. Schiefele, M. Sturla, M. A. H. Vozmediano, *Physics Reports* **2016**, *617*, 1.

[3] Z. Dai, L. Liu, Z. Zhang, *Adv. Mater.* **2019**, *31*, 1805417.

[4] Z. Peng, X. Chen, Y. Fan, D. J. Srolovitz, D. Lei, *Light: Sci. Appl.* **2020**, *9*, 190.

[5] L. Du, T. Hasan, A. Castellanos-Gomez, G.-B. Liu, Y. Yao, C. N. Lau, Z. Sun, *Nature Reviews Physics* **2021**, *3*, 193.

[6] M. Ghorbani-Asl, S. Borini, A. Kuc, T. Heine, *Physical Review B* **2013**, *87*.

[7] L. Kou, C. Tang, Y. Zhang, T. Heine, C. Chen, T. Frauenheim, *J. Phys. Chem. Lett.* **2012**, *3*, 2934.

[8] C. Lee, X. Wei, J. W. Kysar, J. Hone, *Science* **2008**, *321*, 385.

[9] S. Bertolazzi, J. Brivio, A. Kis, *ACS Nano* **2011**, *5*, 9703.

[10] A. Castellanos-Gomez, M. Poot, G. A. Steele, H. S. J. van der Zant, N. Agrait, G. Rubio-Bollinger, *Adv. Mater.* **2012**, *24*, 772.

[11] K. He, C. Poole, K. F. Mak, J. Shan, *Nano Lett.* **2013**, *13*, 2931.

[12] H. J. Conley, B. Wang, J. I. Ziegler, R. F. Haglund, S. T. Pantelides, K. I. Bolotin, *Nano Lett.* **2013**, *13*, 3626.

[13] Y. Y. Hui, X. Liu, W. Jie, N. Y. Chan, J. Hao, Y.-T. Hsu, L.-J. Li, W. Guo, S. P. Lau, *ACS Nano* **2013**, *7*, 7126.

[14] A. Castellanos-Gomez, R. Roldán, E. Cappelluti, M. Buscema, F. Guinea, H. S. J. van der Zant, G. A. Steele, *Nano Lett.* **2013**, *13*, 5361.

[15] F. Carrascoso, H. Li, R. Frisenda, A. Castellanos-Gomez, *Nano Res.* **2020**, *14*, 1698.

[16] L. Mennel, M. M. Furchi, S. Wachter, M. Paur, D. K. Polyushkin, T. Mueller, *Nat. Commun.* **2018**, *9*, 516.

[17] L. Mennel, M. Paur, T. Mueller, *APL Photonics* **2019**, *4*, 034404.

[18] L. Mennel, V. Smejkal, L. Linhart, J. Burgdörfer, F. Libisch, T. Mueller, *Nano Lett.* **2020**, *20*, 4242.

[19] L. Kou, C. Chen, S. C. Smith, *J. Phys. Chem. Lett.* **2015**, *6*, 2794.

[20] H. Liu, A. T. Neal, Z. Zhu, Z. Luo, X. Xu, D. Tománek, P. D. Ye, *ACS Nano* **2014**, *8*, 4033.

[21] W. Ma, P. Alonso-gonzález, S. Li, A. Y. Nikitin, J. Yuan, J. Martín-Sánchez, J. Taboada-Gutiérrez, I. Amenabar, P. Li, S. Vélaz, C. Tollan, Z. Dai, Y. Zhang, S. Sriram, K. Kalantar-Zadeh, S. T. Lee, R. Hillenbrand, Q. Bao, *Nature* **2018**, *562*, 557.

[22] A. Castellanos-Gomez, *J. Phys. Chem. Lett.* **2015**, *6*, 4280.

[23] J. O. Island, R. Biele, M. Barawi, J. M. Clamagirand, J. R. Ares, C. Sánchez, H. S. J. van der Zant, I. J. Ferrer, R. D'Agosta, A. Castellanos-Gomez, *Sci. Rep.* **2016**, *6*, 22214.

[24] J. O. Island, Aday J Molina-Mendoza, Mariam Barawi, Robert Biele, Eduardo Flores, José M Clamagirand, José R Ares, Carlos Sánchez, Herre S J van der Zant, D'AgostaRoberto, FerrerIsabel J, Castellanos-GomezAndres, Electronics and optoelectronics of quasi-1D layered transition metal trichalcogenides, *2D Materials* **2017**, *4*, 022003.

[25] R. Lv, J. A. Robinson, R. E. Schaak, D. Sun, Y. Sun, T. E. Mallouk, M. Terrones, *Acc. Chem. Res.* **2015**, *48*, 56.

[26] A. Lipatov, P. Wilson, M. Shekhirev, J. Teeter, R. Netusil, A. Sinitkii, *Nanoscale* **2015**, *7*, 12291.

[27] W. Zhu, L. Liang, R. H. Roberts, J.-F. Lin, D. Akinwande, *ACS Nano* **2018**, *12*, 12512.

[28] Y. Li, Z. Hu, S. K. Lai, W. Ji, S. P. Lau, *Adv. Funct. Mater.* **2017**, *27*, 1600986.

[29] G. Zhang, S. Huang, A. Chaves, C. Song, V. O. Özçelik, T. Low, H. Yan, *Nat. Commun.* **2017**, *8*, 14071.

[30] W. Luo, A. D. Oyedele, Y. Gu, T. Li, X. Wang, A. V. Haglund, D. Mandrus, A. A. Puretzky, K. Xiao, L. Liang, Xi Ling, *Advanced Functional Materials* **2020**, *30*, 2003215.

[31] Y. Wang, S. Yao, P. Liao, S. Jin, Q. Wang, M. J. Kim, G. J. Cheng, W. Wu, *Adv. Mater.* **2020**, *32*, 2002342.

[32] L. Li, W. Han, L. Pi, P. Niu, J. Han, C. Wang, B. Su, H. Li, Jie Xiong, Y. Bando, T. Zhai, *InfoMat* **2019**, *1*, 54.



- [33] J. Dai, M. Li, X. C. Zeng, *Wiley Interdiscip. Rev.: Comput. Mol. Sci.* **2016**, 6, 211.
- [34] Y. Jin, X. Li, J. Yang, *Phys. Chem. Chem. Phys.* **2015**, 17, 18665.
- [35] J. O. Island, M. Buscema, M. Barawi, J. M. Clamagirand, J. R. Ares, C. Sánchez, I. J. Ferrer, G. A. Steele, H. S. J. van der Zant, A. Castellanos-Gomez, *Advanced Optical Materials* **2014**, 2, 641.
- [36] J. O. Island, M. Barawi, R. Biele, A. Almazán, J. M. Clamagirand, J. R. Ares, C. Sánchez, H. S. J. van der Zant, J. V. Álvarez, R. D'Agosta, I. J. Ferrer, A. Castellanos-Gomez, *Adv. Mater.* **2015**, 27, 2595.
- [37] K. Wu, E. Torun, H. Sahin, B. Chen, X. Fan, A. Pant, D. Parsons Wright, T. Aoki, F. M. Peeters, E. Soignard, S. Tongay, *Nat. Commun.* **2016**, 7, 12952.
- [38] E. Guilmeau, D. Berthebaud, P. R. N. Misse, S. Hébert, O. I. Lebedev, D. Chateigner, C. Martin, A. Maignan, *Chemistry of Materials* **2014**, 26, 5585.
- [39] W.-W. Xiong, J.-Q. Chen, X.-C. Wu, J.-J. Zhu, *J. Mater. Chem. C* **2015**, 3, 1929.
- [40] Z. Zhou, H. Liu, D. Fan, G. Cao, C. Sheng, *ACS Appl. Mater. Interfaces* **2018**, 10, 37031.
- [41] A. Castellanos-Gomez, M. Buscema, R. Molenaar, V. Singh, L. Janssen, H. S. J. van der Zant, G. A. Steele, *2D Materials* **2014**, 1, 011002.
- [42] R. Frisenda, E. Navarro-Moratalla, P. Gant, D. Pérez De Lara, P. Jarillo-Herrero, R. V. Gorbachev, A. Castellanos-Gomez, *Chem. Soc. Rev.* **2018**, 47, 53.
- [43] Q. Zhao, T. Wang, Y. K. Ryu, R. Frisenda, A. Castellanos-Gomez, *Journal of Physics: Materials* **2020**, 3, 016001.
- [44] S. Kurita, M. Tanaka, F. Lévy, *Phys. Rev. B* **1993**, 48, 1356.
- [45] S. Kurita, J. L. Staehli, M. Guzzi, F. Lévy, *Phys. B+C* **1981**, 105, 169.
- [46] R. Frisenda, Y. Niu, P. Gant, A. J. Molina-Mendoza, R. Schmidt, R. Bratschitsch, J. Liu, L. Fu, D. Dumcenco, A. Kis, D. P. De Lara, A. Castellanos-Gomez, *Journal of Physics D: Applied Physics* **2017**, 50, 074002.
- [47] Y. Niu, S. Gonzalez-Abad, R. Frisenda, P. Marauhn, M. Drüppel, P. Gant, R. Schmidt, N. Taghavi, D. Barcons, A. Molina-Mendoza, S. de Vasconcellos, R. Bratschitsch, D. Perez De Lara, M. Röhlfing, A. Castellanos-Gomez, *Nanomaterials* **2018**, 8, 725.
- [48] Y. Li, T. Wang, M. Wu, T. Cao, Y. Chen, R. Sankar, R. K. Ulaganathan, F. Chou, C. Wetzel, C.-Y. Xu, S. G. Louie, S.-F. Shi, *2D Materials* **2018**, 5, 021002.
- [49] C. Song, F. Fan, N. Xuan, S. Huang, G. Zhang, C. Wang, Z. Sun, H. Wu, H. Yan, *ACS Appl. Mater. Interfaces* **2018**, 10, 3994.
- [50] M. Li, J. Dai, X. C. Zeng, *Nanoscale* **2015**, 7, 15385.
- [51] D. R. Hamann, *Physical Review B* **2013**, 88,;
- [52] M. Schlipf, F. Gygi, *Computer Physics Communications* **2015**, 196, 36.
- [53] P. Giannozzi, S. Baroni, N. Bonini, M. Calandra, R. Car, C. Cavazzoni, D. Ceresoli, G. L. Chiarotti, M. Cococcioni, I. Dabo, A. D. Corso, S. de Gironcoli, S. Fabris, G. Fratesi, R. Gebauer, U. Gerstmann, C. Gougoussis, A. Kokalj, M. Lazzeri, L. Martin-Samos, N. Marzari, F. Mauri, R. Mazzarello, S. Paolini, A. Pasquarello, L. Paulatto, C. Sbraccia, S. Scandolo, G. Sclauzero, A. P. Seitsonen, et al., *J. Phys.: Condens. Matter* **2009**, 21, 395502.
- [54] P. Giannozzi, O. Andreussi, T. Brumme, O. Bunau, M. Buongiorno Nardelli, M. Calandra, R. Car, C. Cavazzoni, D. Ceresoli, M. Cococcioni, N. Colonna, I. Carnimeo, A. Dal Corso, S. de Gironcoli, P. Delugas, R. A. DiStasio, A. Ferretti, A. Floris, G. Fratesi, G. Fugallo, R. Gebauer, U. Gerstmann, F. Giustino, T. Gorni, J. Jia, M. Kawamura, H.-Y. Ko, A. Kokalj, E. Küçükbenli, M. Lazzeri, et al., *J. Phys.: Condens. Matter* **2017**, 29, 465901.
- [55] A. Marini, C. Hogan, M. Gruening, D. Varsano, *Comput. Phys. Commun.* **2009**, 180, 1392.
- [56] D. Sangalli, A. Ferretti, H. Miranda, C. Attaccalite, I. Marri, E. Cannuccia, P. Melo, M. Marsili, F. Paleari, A. Marrazzo, G. Prandini, P. Bonfà, M. O. Atambo, F. Affinito, M. Palummo, A. Molina-Sánchez, C. Hogan, M. Grüning, D. Varsano, A. Marini, *J. Phys.: Condens. Matter* **2019**, 31, 325902.